Investigation of transport phenomena and defect formation in pulsed laser keyhole welding of zinc-coated steels

2006 J. Phys. D: Appl. Phys. 39 5338

(http://iopscience.iop.org/0022-3727/39/24/036)

INSTITUTE OF PHYSICS PUBLISHING JOURNAL OF PHYSICS D: APPLIED PHYSICS

J. Phys. D: Appl. Phys. **39** (2006) 5338–5355 doi:10.1088/0022-3727/39/24/036

Investigation of transport phenomena and defect formation in pulsed laser keyhole welding of zinc-coated steels

J Zhou[1], H L Tsai[2] and T F Lehnhoff[2]

[1] Department of Mechanical and Engineering Technology, Georgia Southern University, PO Box 8046, Statesboro, GA 30460, USA
[2] Department of Mechanical and Aerospace Engineering, University of Missouri–Rolla, 1870 Miner Circle, Rolla, MO 65409, USA

E-mail: jzhou@georgiasouthern.edu

Received 21 April 2006, in final form 25 October 2006
Published 1 December 2006
Online at stacks.iop.org/JPhysD/39/5338

Abstract

Lasers are being used to weld zinc-coated steels due to high welding speed, high aspect ratio, and narrow heat affected zone. However, escape of high-pressure zinc vapour in the welding process can damage the weld pool continuity and cause large voids and serious undercuts in the final welds. In this paper, a mathematical model and the associated numerical techniques have been developed to study the transport phenomena and defect formation mechanisms in pulsed laser keyhole welding of zinc-coated steels. The volume-of-fluid (VOF) method is employed to track free surfaces. The continuum model is used to handle the liquid phase, the solid phase and the mushy zone of the metal. The enthalpy method is employed to account for the latent heat during melting and solidification. The transient heat transfer and melt flow in the weld pool during the keyhole formation and collapse processes are calculated. The escape of zinc vapour through the keyhole and the interaction between zinc vapour and weld pool are studied. Voids in the welds are found to be caused by the combined effects of zinc vapour–melt interactions, keyhole collapse and solidification process. By controlling the laser pulse profile, it is found that the keyhole collapse and solidification process can be delayed, allowing the zinc vapour to escape, which results in the reduction or elimination of voids. The good agreement between the model predictions and the experimental observations indicates that the proposed model lays a solid foundation for future study of laser welding of zinc-coated steels.

(Some figures in this article are in colour only in the electronic version)

1. Introduction

Zinc-coated steels are widely used in various industries because of their low prices and high corrosion resistance. Laser welding has been used to join zinc-coated steels for its significant savings in weight, manufacturing time and cost [1]. In laser welding of zinc-coated steels in lap configuration, a problem results from the presence of zinc with a low boiling point (∼906 °C), which is much lower than the melting temperature of steel (∼1530 °C). As a result, the zinc-coatings at the interface of the two metal sheets are heated to the boiling point and vaporized. This 'zinc-vapour' occupies a much larger volume than the original zinc coatings. If the amount of zinc vapour produced can be properly vented away, then there is no problem. But, if the zinc vapour has no way to escape during the welding process, then the pressure of this zinc vapour can become very high until the vapour is vented through the molten pool. This can cause exposition of molten metal leading to blowholes, an unstable weld pool, pores and rough surfaces [2, 3].

Several ideas have been proposed to get a sound weld quality for laser welding of zinc-coated steels. One idea is

to create a gap between the two metal sheets during welding [4–6]. This approach allows the zinc vapours to escape through the gap instead of through the weld pool. Although, the gap method has been proven to improve weld quality in the laser lap welding of zinc-coated steels, it is difficult to maintain such a controlled gap in a production environment. Usually, gaps are not desirable in laser welding of lap joints because they can lead to undercuts and corresponding decrease in the mechanical properties of the weld joint. Some ideas were proposed to conduct welding after the removal of the zinc coating [4,7,8]. While successful, this approach is costly and not practical for industrial applications. Another approach is to control the formation and interaction of the zinc vapour during the welding process by using various shielding gases [4,9,10]. These approaches proved inconsistent. Some researchers have investigated the impact of power density and distribution and lap configurations [11–14]. This approach also had little impact on the weld-ability of zinc-coated steels. Several researchers are investigating new laser technologies, such as dual-beam laser welding and hybrid laser welding [15,16]. But their feasibility is still under study. Recently, some researchers reported that a gap is not necessary in lap laser welding of a zinc-coated steel sheet by using pulsed lasers [1,7,17]. They claimed that if a stable keyhole can be maintained during the welding process, the zinc vapour formed during laser welding processes can escape through the keyhole and a very sound weld can be achieved. The underlying mechanisms for the success of this method still need further investigation.

In order to optimize the laser welding process and obtain a good quality weld, it is necessary to have a good understanding of the defect formation mechanisms associated with laser welding of zinc-coated steels. Xie and Denney [18] investigated the possibility of using dual laser beams to reduce the weld defects in laser welding of zinc-coated steels. Their experimental results show that a sound weld can be achieved and there is a relationship between several variables which have an impact on reducing weld defects. These variables include power density, spot size, inter-beam space and focal length. However, the relationship between the variables and the reasons for the success still need more investigation. Tzeng [1,13] studied the feasibility of pulsed laser beam welding of zinc-coated steels in lap configuration using Lumonics JK 701 Nd : YAG laser. He pointed out that by optimizing the process parameters, such as average peak power density, pulse duration and welding speed, good quality lap welds with no porosity are made consistently and easily when there is no gap between the metal sheets. The experimental results also suggest that the effect of pulse duration is closely associated with the balance between the keyhole effect and the vapour production within the molten metal. Katayama *et al* [17] experimentally investigated the laser weld-ability of zinc-coated steels. Furthermore, porosity formation mechanisms of characteristic welds were investigated by ultra-high speed video observation and micro-focused x-ray transmission imaging of welding phenomena. Based on the results of observation and analysis, they concluded that lap welding of zinc-coated steels with no gap is possible by using a pulsed laser and the welding defects are strongly associated with the weld pool shape. Gu and Mueller [16] used the laser-TIG hybrid technique to weld zinc-coated steels and porosity-free welds were achieved. It is believed that the success of this

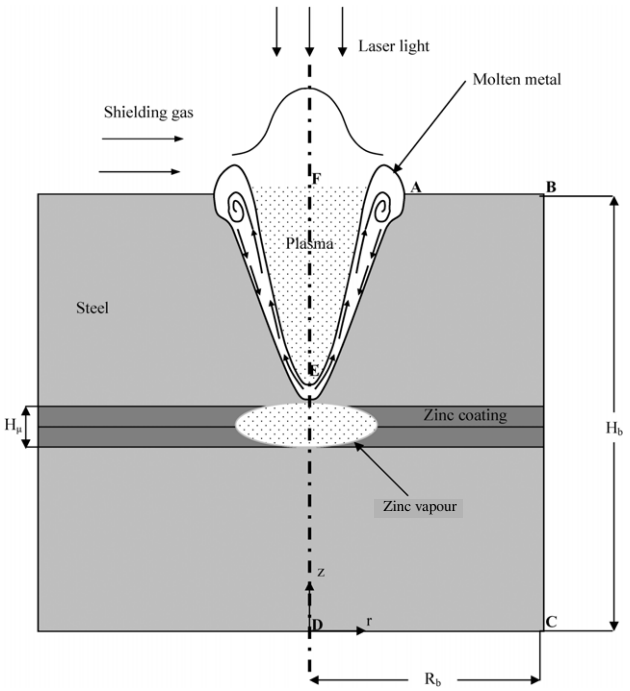

Figure 1. Schematic sketch of a pulsed laser keyhole welding of zinc-coated steels (not to scale).

method is due to the use of a TIG arc, which can help to stabilize the weld pool and produce a suitable keyhole. Welding defects are found to be related to the fluid flow in the welding pool. According Matsunawa *et al* [19] and Katayama *et al* [20], the formation of cavities and porosities result from keyhole instability and the melt movements inside it. Some porosity appears to be due to the trapped zinc vapour.

Though there has been a lot of research focused on the mechanism of laser welding of steels, most of the research on laser welding of zinc-coated steels is experimentally carried out. Although some experimental equipment such as the micro-focused x-ray transmission imaging system can provide some useful information about defect formation, the true mechanism of defect formation is based largely on conjecture. The velocity field, the temperature field and the interaction between zinc vapour and weld pool during zinc vapour escape and keyhole collapse processes are not known, which are key factors for understanding the mechanisms of defect formation. Numerical simulation of keyhole mode laser welding of zinc-coated steels can give us an idea about what happens during the welding process. In this study, a comprehensive model has been set up for pulsed laser welding of zinc-coated steels. The model includes the calculations of temperature field, pressure balance, melt flow, free surface, laser-induced plasma, zinc vapour formation, zinc vapour escape and zinc vapour interaction with the weld pool. Also, the defect formation mechanisms and feasibility of getting sound welds by controlling the laser pulse shape are investigated.

2. Mathematical model

Figure 1 shows a schematic sketch of a pulsed laser keyhole welding process. A control volume method employing the volume-of-fluid (VOF) technique [21] and the continuum

formulation [22] is used to calculate the momentum and energy transport in the weld pool. The VOF technique can handle a transient deformed weld pool surface, while the continuum formulation can handle fusion and solidification for the liquid region, the mush zone and the solid region. Plasma in the keyhole is treated as the vapour of weld material. Although the velocity and pressure change dramatically across the Knudsen layer, the generic translation vapour flow along the keyhole is neglected [23] and, in the present study, only the temperature distribution is considered. Meanwhile, the pressure along the keyhole is also considered to be approximately constant [24] and is comparable to the atmospheric pressure.

2.1. Metal zone simulation

2.1.1. Governing equations. The governing differential equations used to describe the heat and mass transfer and fluid flow in a cylindrical coordinate (r–z) system given by Chiang and Tsai [22] are modified and used in the present study:

Continuity

$$\frac{\partial}{\partial t}(\rho) + \nabla \cdot (\rho V) = 0. \tag{1}$$

Momentum

$$\frac{\partial}{\partial t}(\rho u) + \nabla \cdot (\rho \boldsymbol{V} u) = \nabla \cdot \left(\mu_{\mathrm{l}} \frac{\rho}{\rho_{\mathrm{l}}} \nabla u\right) - \frac{\partial P}{\partial r} - \frac{u_{\mathrm{l}}}{K} \frac{\rho}{\rho_{\mathrm{l}}}(u - u_{\mathrm{s}}) - \frac{C\rho^2}{K^{0.5}\rho_{\mathrm{l}}}|u - u_{\mathrm{s}}|(u - u_{\mathrm{s}}) - \nabla \cdot (\rho f_{\mathrm{s}} f_{\mathrm{l}} \boldsymbol{V}_{\mathbf{r}} u_{\mathrm{r}}) + \nabla \cdot \left(\mu_{\mathrm{s}} u \nabla \left(\frac{\rho}{\rho_{\mathrm{l}}}\right)\right), \tag{2}$$

$$\frac{\partial}{\partial t}(\rho v) + \nabla \cdot (\rho \boldsymbol{V} v) = \rho g + \nabla \cdot \left(\mu_{\mathrm{l}} \frac{\rho}{\rho_{\mathrm{l}}} \nabla v\right) - \frac{\partial P}{\partial z} - \frac{v_{\mathrm{l}}}{K} \frac{\rho}{\rho_{\mathrm{l}}}(v - v_{\mathrm{s}}) - \frac{C\rho^2}{K^{0.5}\rho_{\mathrm{l}}}|v - v_{\mathrm{s}}|(v - v_{\mathrm{s}}) - \nabla \cdot (\rho f_{\mathrm{s}} f_{\mathrm{l}} \boldsymbol{V}_{\mathbf{r}} v_{\mathrm{r}}) + \nabla \cdot \left(\mu_{\mathrm{s}} v \nabla \left(\frac{\rho}{\rho_{\mathrm{l}}}\right)\right) + \rho g \beta_{\mathrm{T}}(T - T_0). \tag{3}$$

Energy

$$\frac{\partial}{\partial t}(\rho h) + \nabla \cdot (\rho \boldsymbol{V} h) = \nabla \cdot \left(\frac{k}{c_p} \nabla h\right) - \nabla \cdot \left(\frac{k}{c_p} \nabla (h_{\mathrm{s}} - h)\right) - \nabla \cdot (\rho(\boldsymbol{V} - \boldsymbol{V}_{\mathbf{s}})(h_{\mathrm{l}} - h)). \tag{4}$$

The physical meaning of each term appearing in the above equations can be found in [22]. In equations (1)–(4), the continuum density, specific heat, thermal conductivity, solid mass fraction, liquid mass fraction, velocity and enthalpy are defined in [25].

2.2. Tracking of free surfaces

The algorithm of VOF is used to track the dynamics of free surfaces [21]. The fluid configuration is defined by a VOF, $F(r, z, t)$, which tracks the location of free surface. The function F takes the value of one for the cell full of fluid and the value of zero for the empty cell. Cells with F values between zero and one are partially filled with fluid and identified as surface cells. The function F is governed by the following equation:

$$\frac{\mathrm{d}F}{\mathrm{d}t} = \frac{\partial F}{\partial t} + (\boldsymbol{V} \cdot \nabla)F = 0. \tag{5}$$

2.3. Boundary conditions

The boundaries of the metal zone simulation are divided into five segments, as shown in figure 1.

a. Top surface inside the keyhole (AE in figure 1). For cells containing free surface, that is, cells that contain fluid but have one or more empty neighbours, in the direction normal to the free surface, the following pressure condition must be satisfied [26, 27]:

$$P = P_\sigma + P_{\mathrm{r}}, \tag{6}$$

where P is the pressure at the free surface in a direction normal to the local free surface. P_σ is the surface tension and P_{r} is the recoil pressure. P_σ is calculated by the following formula:

$$P_\sigma = \kappa\gamma, \tag{7}$$

where κ is the free surface curvature, given by [22]

$$\kappa = -\left[\nabla \cdot \left(\frac{\vec{n}}{|\vec{n}|}\right)\right] = \frac{1}{|\vec{n}|}\left[\left(\frac{\vec{n}}{|\vec{n}|} \cdot \nabla\right)|\vec{n}| - (\nabla \cdot \vec{n})\right], \tag{8}$$

where $\vec{n}$ is the unit vector normal to the local free surface. For a pseudo-binary Fe–S system, the surface tension coefficient γ can be calculated as a function of temperature T and sulfur concentration f^α [28]:

$$\gamma = 1.943 - 4.3 \times 10^{-4}(T - 1723) - RT \times 1.3 \times 10^{-8} \times \ln\left[1 + 0.00318 f^\alpha \exp\left(\frac{1.66 \times 10^8}{RT}\right)\right]. \tag{9}$$

In this study, the sulfur concentration is assumed to be constant, and the temperature-dependent Marangoni shear stress on the free surface in the direction tangential to the local surface is given by [29]

$$\tau_{\vec{s}} = \mu_{\mathrm{l}} \frac{\partial(\boldsymbol{V} \cdot \vec{s})}{\partial \vec{n}} = \frac{\partial \gamma}{\partial T} \frac{\partial T}{\partial \vec{s}}. \tag{10}$$

Calculation of the evaporation-induced recoil pressure P_{r} is complicated by the existence of a Knudsen layer over the vaporizing surface. Based on Knight's model [30], the recoil pressure can be calculated by [31]

$$P_{\mathrm{r}} = AB_0/\sqrt{T_{\mathrm{w}}} \exp(-U/T_{\mathrm{w}}), \tag{11}$$

where A is the numerical coefficient and B_0 is the vaporization constant. The coefficient A depends on the ambient pressure and its value varies from 0.55 for evaporation in the vacuum to 1 for the case of evaporation under a high ambient pressure. For atmospheric pressure, the coefficient A is close to its minimal value of 0.55. B_0 is at the value of 1.78×10^{10}. T_{w} is the surface temperature of the liquid metal on the keyhole wall. The parameter U is defined as follows [31]:

$$U = m_{\mathrm{a}} H_{\mathrm{v}}/(N_{\mathrm{a}} k_{\mathrm{b}}), \tag{12}$$

where m_{a} is atomic mass, H_{v} is the latent heat of evaporation, N_{a} is the Avogadro's number and k_{b} is the Boltzmann constant.

The energy on the top free surface is balanced between laser irradiation, plasma-keyhole wall radiation, the heat dissipation through convection and metal vaporization. In general, since the velocity of the plume along the surface is

Table 1. Thermophysical properties of 304 stainless steel and process parameters.

Nomenclature	Value
Specific heat of solid phase, c_s (J kg^{-1} K^{-1})	700
Specific heat of liquid phase, c_l(J kg^{-1} K^{-1})	780
Thermal conductivity of solid phase, k_s (W m^{-1} K^{-1})	22
Thermal conductivity of liquid phase, k_l (W m^{-1} K^{-1})	22
Density of solid phase, ρ_s (kg m^{-3})	7200
Density of liquid phase, ρ_l (kg m^{-3})	6900
Dynamic viscosity, μ_l (kg m^{-1} s^{-1})	0.006
Latent heat of fusion, H (J kg^{-1})	2.47×10^5
Solidus temperature, T_s (K)	1670
Liquidus temperature, T_l (K)	1727
Boiling temperature, T_v (K)	3375
Latent heat of vaporization, H_v (J kg^{-1})	6.34×10^6
Laser power, P (kW)	2.0
Laser beam radius at focus, r_{f0} (mm)	0.25
Laser beam radius, r_f (mm)	0.25
Substrate initial temperature, T_0 (K)	300
Surrounding temperature, T_{gas} (K)	300
Ambient temperature, T_∞ (K)	300
Thickness of substrate metal, H_b (mm)	4.0
Radius of substrate metal, R_b (mm)	10.0
Substrate sulfur concentration, C_s (ppm)	100
Atmospheric pressure, P_{atm} (Pa)	1.013×10^5
Gas constant, R (J kg^{-1} mole^{-1})	8.3×10^3
Average ionic charge in the plasma, Z	1
Angular frequency of the laser radiation, ω (rad s^{-1})	1.78×10^{14}
Quantum mechanical Gaunt factor, $\bar{g}$	1.5
Excitation temperature, T_e (K)	9×10^3
Degeneracy factors for ions, g_i	30
Degeneracy factors for neutral atoms, g_0	25
Degeneracy factors for electrons, g_e	30
Speed of light, c (m s^{-1})	3×10^8
Boltzmann's constant, k (J K^{-1})	1.38×10^{-23}
Planck's constant, h (J s)	6.625×10^{-34}

assumed to be zero [23], the heat loss due to convection is omitted. The energy balance is given by the following formula:

$$k\frac{\partial T}{\partial \vec{n}} = q_{laser} + q_{rad} - q_{evap}. \tag{13}$$

In this study, the liquid/vapour evaporation model is used due to the low intensity of laser irradiation. The heat loss due to surface evaporation can be written as [32]

$$q_{evap} = W H_v, \tag{14}$$

$$\log(W) = A_v + \left(6.121 - \frac{18836}{T}\right) - 0.5 \log\ T. \tag{15}$$

The laser heat flux q_{laser} comes from the Fresnel absorption of the incident intensity directly from the laser beam plus the incident intensity from the multiple reflections:

$$q_{laser} = I_o(r, z)\alpha_{Fr}(\varphi_o) + \sum_{m=1}^{n} I_{r,m}(r, z)\alpha_{Fr}(\varphi_m), \tag{16}$$

$$\alpha_{Fr}(\varphi) = 1 - \frac{1}{2}\left(\frac{1 + (1 - \varepsilon_f \cos\ \varphi)^2}{1 + (1 + \varepsilon_f \cos\ \varphi)^2} + \frac{\varepsilon_f^2 - 2\varepsilon_f \cos\ \varphi + 2\cos^2\varphi}{\varepsilon_f^2 + 2\varepsilon_f \cos\ \varphi + 2\cos^2\varphi}\right), \tag{17}$$

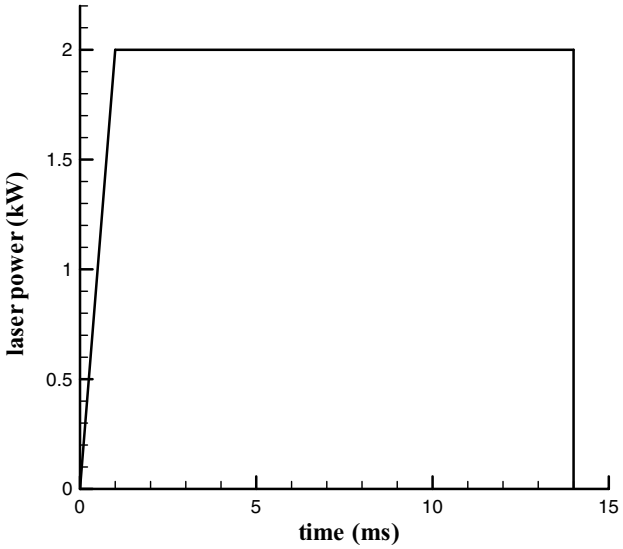

Figure 2. Laser pulse used in laser welding of zinc-coated steels.

where φ is the angle of the incident light with the normal of the keyhole surface and n is the total number of incident light from multiple reflections. ε_f is a material-dependent coefficient. In CO_2 laser welding of mild steel, $\varepsilon_f = 0.2$, is used. $I_o(r, z)$ and $I_{r,m}(r, z)$ are, respectively, the incident intensity from the laser beam and the mth multiple reflection at the keyhole wall which are given as

$$I_o(r, z) = I_c(r) \exp\left(-\int_0^{z_o} K_{pl}\, dz\right), \tag{18}$$

$$I_{r,m}(r, z) = I_r(r, z) \exp\left(-\int_0^{z_m} K_{pl}\, dz\right), \tag{19}$$

$$I_r(r, z) = I_o(r, z)(1 - \alpha_{Fr}), \tag{20}$$

where $I_c(r)$ stands for the original collimated incident laser beam intensity, $I_{r,m}(r, z)$ is the reflected laser beam intensity at m times reflections, $\int_0^{z_o} K_{pl}\, dz$ and $\int_0^{z_m} K_{pl}\, dz$ are the optical thickness of the laser transportation path, respectively, for the first incident and the multiple reflections and K_{pl} is the plasma absorption coefficient due to the inverse bremsstrahlung (IB) absorption [33]

$$K_{pl} = \frac{n_e n_i Z^2 e^6 2\pi}{6\sqrt{3} m \varepsilon_0^3 c \bar{h} \omega^3 m_e^2} \left(\frac{m_e}{2\pi k_b T_{pl}}\right)^{0.5} \times \left[1 - \exp\left(-\frac{\omega}{k_b T_{pl}}\right)\right] \bar{g}, \tag{21}$$

where Z is the charge of ion in the plasma, e is the charge of the electron, ω is the angular frequency of the laser irradiation, ε_0 is the dielectric constant, n_e and n_i are the densities of electrons and ions respectively, $\bar{h}$ is Planck's constant, m_e is the electron mass, T_{pl} is the plasma temperature, c is the speed of light and $\bar{g}$ is the quantum mechanical Gaunt factor. For weakly ionized plasma in the keyhole, the Saha equation [34] can be used to calculate the densities of the plasma species:

$$\frac{n_e n_i}{n_0} = \frac{g_e g_i}{g_0} \frac{(2\pi m_e k_b T_{pl})^{1.5}}{\bar{h}^3} \exp\left(-\frac{E_i}{k_b T_{pl}}\right), \tag{22}$$

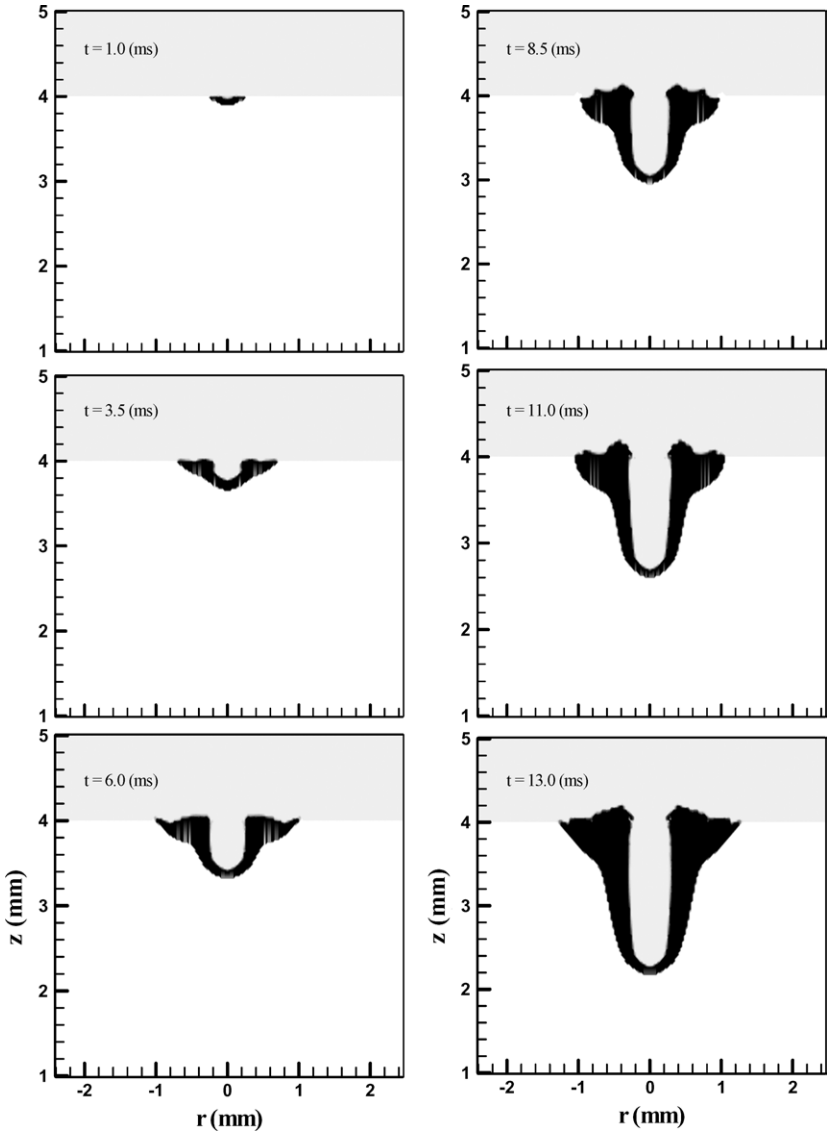

Figure 3. A sequence of weld pool evolution during keyhole formation.

where n_0 is neutral particle density which is $10^{26}\,\mathrm{cm}^{-3}$ for iron [34], g_e, g_i and g_0 are, respectively, the degeneracy factors for electrons, ions and neutral atoms and E_i is the ionization potential for the neutral atoms in the gas. Assuming the laser intensity distribution is ideal Gaussian-like, $I_c(r)$ can be written as [35]

$$I_c(r) = \frac{2P_{\mathrm{laser}}}{\pi r_{\mathrm{fo}}^2}\left(\frac{r_f}{r_{\mathrm{fo}}}\right)^2 \exp\left(-\frac{2r^2}{r_f^2}\right), \tag{23}$$

where r_f is the beam radius, r_{fo} is the beam radius at the focal position and P_{laser} is the laser power. In laser welding, the keyhole surface temperature is much lower than that of the plasma, so the radiation and emission of the surface can be omitted. Then q_{rad} can be simplified as

$$q_{\mathrm{rad}} = \varepsilon\sigma(\overline{T_{\mathrm{pl}}}^4 - T^4), \tag{24}$$

where $\overline{T_{\mathrm{pl}}}$ is the average temperature of keyhole plasma.

b. Top surface outside the keyhole (AB in figure 1). Boundary condition on the top surface outside the keyhole is similar to that inside the keyhole. The differences lie in the absence of plasma and multiple reflections. As shown in figure 1, there is a shielding gas flow above the base metal, which means that plasma outside the keyhole will be blown away. So equation (16) can be written as

$$q_{\mathrm{laser}} = I_o(r, z)\alpha_{\mathrm{Fr}}\cos\,\varphi. \tag{25}$$

Since there is no plasma and the temperature of shielding gas is much lower than that of the metal surface, the radiation heat flux can be given as

$$q_{\mathrm{rad}} = -\varepsilon\sigma(T^4 - T_\infty^4). \tag{26}$$

Here, T_∞ is the ambient temperature. Since there is a shielding gas flow over the surface, the convection heat loss cannot be omitted which is given by

$$q_{\mathrm{conv}} = h_{\mathrm{conv}}(T - T_\infty). \tag{27}$$

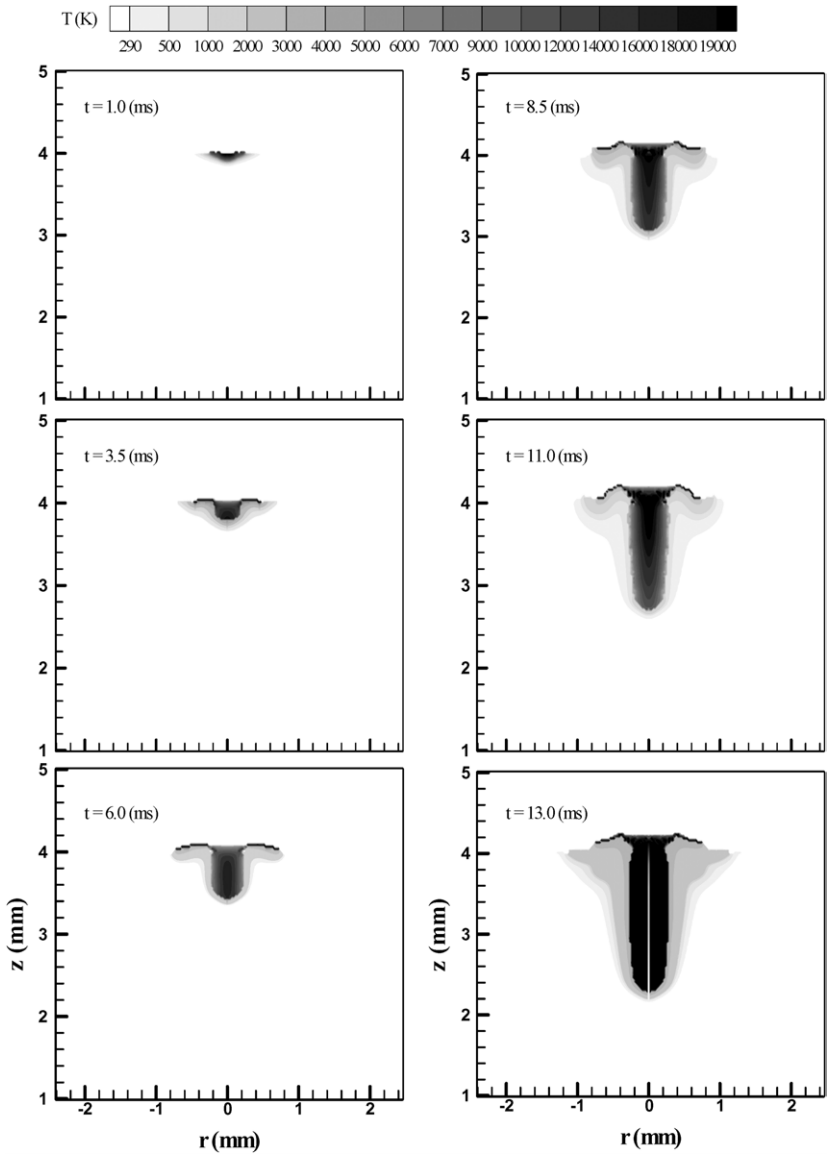

Figure 4. The corresponding temperature distributions for the sequence shown in figure 3.

c. Side surface (BC in figure 1).

$$-k\frac{\partial T}{\partial r} = q_{\text{conv}}, \tag{28}$$

$$u = 0, \qquad v = 0. \tag{29}$$

d. Bottom surface (CD in figure 1).

$$-k\frac{\partial T}{\partial z} = q_{\text{conv}}, \tag{30}$$

$$u = 0, \qquad v = 0. \tag{31}$$

e. Symmetrical axis (DE in figure 1).

$$\frac{\partial T}{\partial r} = 0, \tag{32}$$

$$u = 0, \qquad \frac{\partial v}{\partial r} = 0. \tag{33}$$

2.4. Plasma zone simulation

2.4.1. Governing equations. In the current study, before the zinc vapour escapes into the keyhole, metal vapour in the keyhole is assumed to be a compressible, inviscid ideal gas. Since the heat production by viscous dissipation is rather small in laser welding, the energy equation can be simplified as [36]

$$\begin{aligned}\frac{\partial}{\partial t}(\rho_{\text{pl}} h_{\text{pl}}) = {} & \nabla \cdot \left(\frac{k_{\text{pl}}}{c_{\text{pl}}}\nabla h_{\text{pl}} - \boldsymbol{q}_{\mathbf{r}}\right) \\ & + K_{\text{pl}} I_{\text{c}}(r) \exp\left(-\int_0^{z_o} K_{\text{pl}}\,\mathrm{d}z\right) \\ & + \sum_{m=1}^{n} K_{\text{pl}} I_{\text{r},m}(r, z) \exp\left(-\int_0^{z_m} K_{\text{pl}}\,\mathrm{d}z\right),\end{aligned} \tag{34}$$

where h_{pl} and ρ_{pl} represent, respectively, the enthalpy and density of the plasma and k_{pl} and c_{pl} represent, respectively, the thermal conductivity and specific heat of the plasma. $\boldsymbol{q}_r$ stands for the radiation heat flux vector. Note $h_{\text{pl}} = c_{\text{pl}} T_{\text{pl}}$.

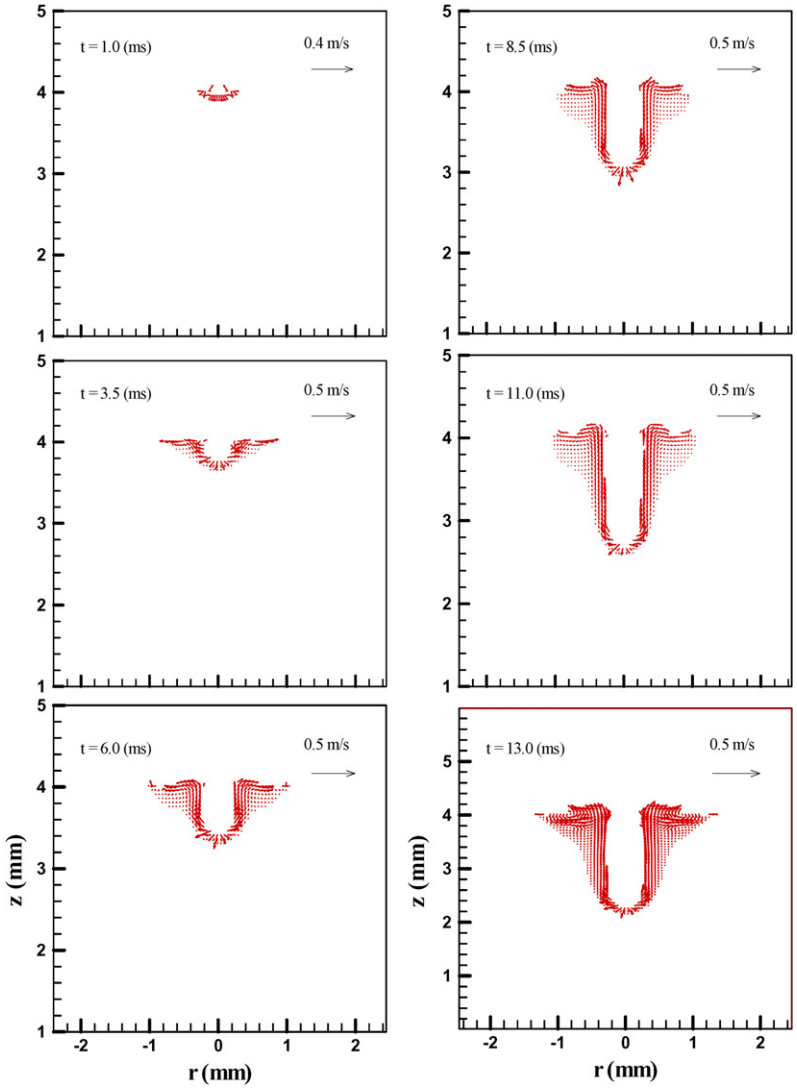

Figure 5. The corresponding temperature distributions as shown in figure 3.

The radiation source term $\nabla \cdot (\boldsymbol{q}_r)$ is defined as

$$\nabla \cdot \boldsymbol{q}_r = k_\mathrm{a}\left(4\pi I_\mathrm{b} - \int_{4\pi} I \,\mathrm{d}\Omega\right), \tag{35}$$

where k_a, I_b and Ω denote the Planck mean absorption coefficient, blackbody emission intensity ($I_\mathrm{b} = \sigma T_\mathrm{pl}^4$) and solid angle, respectively. When an intense laser pulse interacts with the vapour in the keyhole, a significant amount of laser irradiation is absorbed by the ionized particles through the IB absorption. For simplicity, the plasma is assumed to be an absorbing–emitting medium and the scattering effect is neglected. The radiation transport equation (RTE) has to be solved for the total directional radiative intensity $I(\boldsymbol{r}, \boldsymbol{s})$ [37]:

$$(\boldsymbol{s} \cdot \nabla) I(\boldsymbol{r}, \boldsymbol{s}) = k_\mathrm{a}(I_\mathrm{b} - I(\boldsymbol{r}, \boldsymbol{s})), \tag{36}$$

where $\boldsymbol{s}$ and $\boldsymbol{r}$ denote a unit vector along the direction of the radiation intensity and the local position vector. When the plume within the keyhole is weakly ionized, the absorption mechanism mainly depends on electron–neutral interaction and the plume behaves as an optically thin medium. For the evaluation of the intensity and heat flux divergence, the Planck mean absorption coefficient is given as [37]

$$k_\mathrm{a} = \left(\frac{128}{27} k_\mathrm{b}\right)^{0.5} \left(\frac{\pi}{m_\mathrm{e}}\right)^{1.5} \frac{Z^2 e^6 \bar{g}}{h\sigma c^3} \frac{n_\mathrm{e} n_\mathrm{i}}{T_\mathrm{pl}^{3.5}}. \tag{37}$$

2.4.2. Boundary conditions.

a. Bottom surface inside the keyhole (EA in figure 1). Close to the liquid wall inside the keyhole, there is a so-called Knudsen layer where vaporization of material takes place. The vapour temperature across the Knudsen layer is discontinuous, which can be calculated by the following formula [30]:

$$\frac{T_\mathrm{K}}{T_\mathrm{l}} = \left[\sqrt{1 + \pi\left(\frac{\gamma_\mathrm{r} - 1}{\gamma_\mathrm{r} + 1}\frac{m_\mathrm{v}}{2}\right)^2} - \sqrt{\pi}\frac{\gamma_\mathrm{r} - 1}{\gamma_\mathrm{r} + 1}\frac{m_\mathrm{v}}{2}\right]^2, \tag{38}$$

$$m_\mathrm{v} = M_\mathrm{k}\sqrt{\frac{2}{\gamma_\mathrm{r}}}, \tag{39}$$

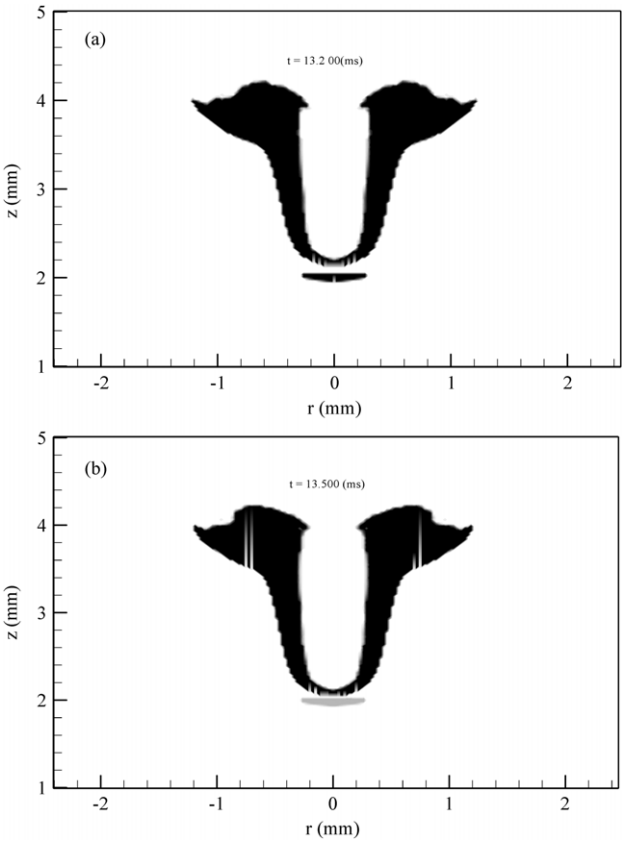

Figure 6. (*a*) The melting of zinc coating and (*b*) the formation of zinc vapour.

where T_K is the vapour temperature outside the Knudsen layer, T_l is the liquid surface temperature adjacent to the Knudsen layer, M_k is the Mach number at the outer of the Knudsen layer and γ_r is the specific heat ratio. The value of m_v depends on the gas dynamics of the vapour flow away from the surface. $M_k = 1.2$ is used in the present study [29]. The vapour is assumed to be iron in the form of monatomic gas with molecular weight of 56, and $\gamma_r = 1.67$. The gas temperature outside the Knudsen layer is used as the boundary temperature. So the boundary condition is given by [37]

$$T_{pl} = T_K, \tag{40}$$

$$I = \varepsilon I_b + \frac{1-\varepsilon}{\pi} \int_{\vec{n}\cdot\Omega'<0} I|\vec{n}\cdot\Omega|d\Omega'. \tag{41}$$

b. Top surface outside the keyhole (FA in figure 1) .

$$T_{pl} = T_\infty, \tag{42}$$

$$I = I_c(r). \tag{43}$$

c. Symmetrical axis (EF in figure 1) .

$$\frac{\partial T_{pl}}{\partial r} = 0, \tag{44}$$

$$\frac{\partial I}{\partial r} = 0. \tag{45}$$

2.5. Zinc vapour simulation

2.5.1. Governing equations. In the welding process, since the melting point of zinc is very low (around 906 °C) compared with that of 304 steel (around 1530 °C), the zinc coating at the interface will be melted first. When the keyhole reaches a certain depth, the accumulated high-pressure zinc vapour on the interface will escape into the keyhole. During its escaping process, the zinc vapour flow is considered as an incompressible viscid fluid flow and the following equations have been used to describe it.

Continuity

$$\nabla \cdot (\boldsymbol{V}_{Zn}) = 0. \tag{46}$$

Momentum

$$\frac{\partial}{\partial t}(\rho_{Zn} u_{Zn}) + \nabla \cdot (\rho_{Zn} \boldsymbol{V}_{Zn} u_{Zn}) = -\frac{\partial P_{Zn}}{\partial r} + \nabla \cdot (\mu_{Zn} \nabla u_{Zn}), \tag{47}$$

$$\frac{\partial}{\partial t}(\rho_{Zn} v_{Zn}) + \nabla \cdot (\rho_{Zn} \boldsymbol{V}_{Zn} v_{Zn}) = -\frac{\partial P_{Zn}}{\partial z} + \nabla \cdot (\mu_{Zn} \nabla v_{Zn}) + \rho_{Zn} g \beta_T (T_{Zn} - T_\infty), \tag{48}$$

where ρ_{Zn} and μ_{Zn} represent the density and viscosity of the zinc vapour, u_{Zn} and v_{Zn} are the velocity distribution in the r- and z-directions separately, $ß_T$ is the thermal expansion coefficient and $\boldsymbol{V}_{Zn}$ stands for the velocity vector of zinc vapour.

2.5.2. Boundary conditions.

a. Bottom surface inside the keyhole (EA in figure 1)

$$u_{Zn} = u, \qquad v_{Zn} = v. \tag{49}$$

b. Top surface outside the keyhole (FA in figure 1)

$$u_{Zn} = 0, \qquad \frac{\partial v_{Zn}}{\partial z} = 0. \tag{50}$$

c. Symmetrical axis (EF in figure 1)

$$u_{Zn} = 0, \qquad \frac{\partial v_{Zn}}{\partial r} = 0. \tag{51}$$

d. Inlet boundary

$$u_{Zn} = 0, \qquad v_{Zn} = \sqrt{\frac{2\rho g h_{keyhole}}{\rho_{zn}}}, \tag{52}$$

$$\rho_{Zn} = \frac{M_{Zn} p_{Zn}}{R T_{Zn}}, \tag{53}$$

$$p_{Zn} = \exp(A_0 \cdot T_{Zn}^{-1} + B \cdot \log(T_{Zn}) + C_0 \cdot T_{Zn} + D_0), \tag{54}$$

where $A_0 = -6620$, $B = -1.255$, $C_0 = 0$, $D_0 = 12.34$. M_{Zn} is the atomic weight of zinc and R is the gas constant.

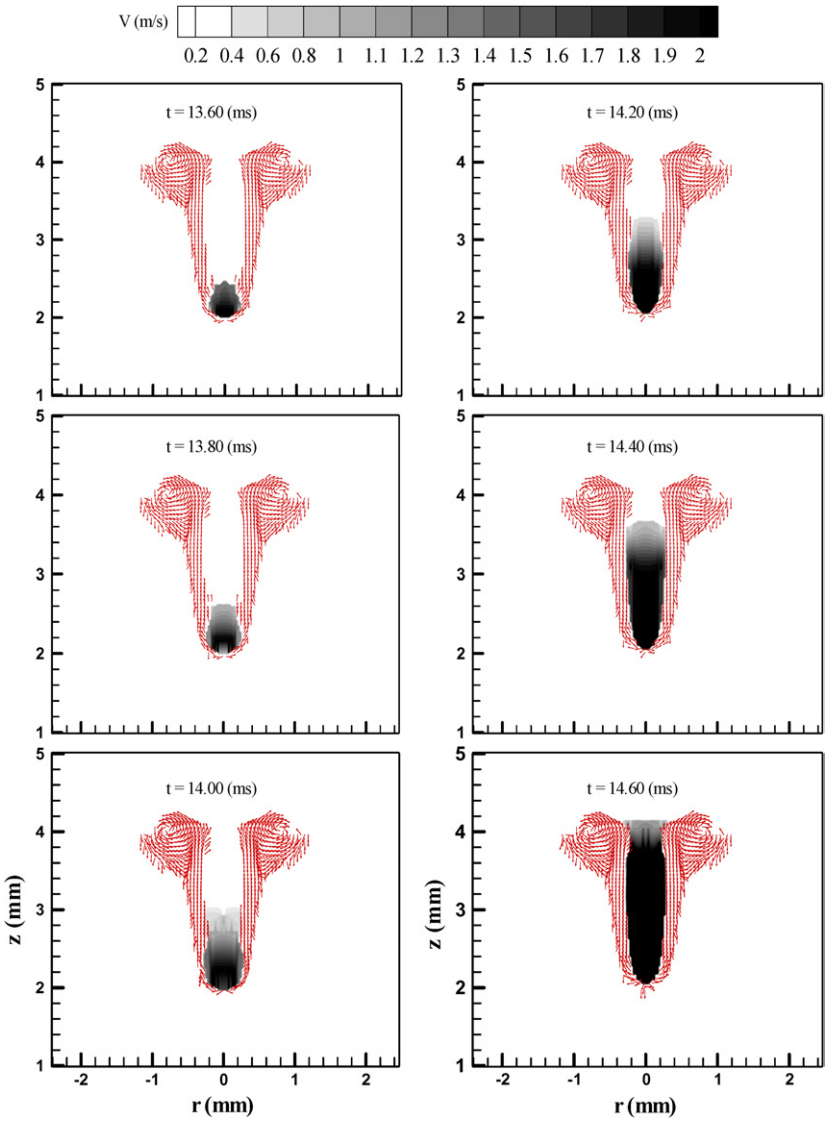

Figure 7. The escaping of zinc vapour via keyhole.

3. Numerical methods

The solutions of transport equations in the metal zone and in the plasma zone are coupled; that is, the simulations of the metal and the plasma zone provide boundary conditions for each other. However, there are large spatial and physical differences between the metal and the plasma zone. To enhance convergence rate and save calculation time, different time and space resolutions are used for the metal and the plasma zone. The governing equations (equations (1)–(4), equation (34) and equations (46)–(48)) and all related supplemental equations and boundary conditions are solved through the following iterative scheme.

1. Equations (1)–(4) are solved iteratively for the metal zone to obtain velocity, pressure and temperature distributions using the associated boundary conditions.
2. Before the zinc vapour escapes into the keyhole, equation (34) is solved iteratively to obtain the plasma temperature distributions in the keyhole under the associated boundary conditions. The steps for solving equation (34) are listed below.
   (a) Solve equation (36) using the associated boundary conditions to get the total directional radiative intensity distributions.
   (b) Solve equation (35) to get radiation source term $\nabla \cdot (\boldsymbol{q}_r)$.
   (c) Solve equations (22) and (21) in the order using the most recent plasma temperature from the previous time step to get the updated plasma absorption coefficient K_{pl}.
   (d) Solve equation (34) to get the updated plasma temperature.
3. Solve VOF algorithm equation (5) to obtain the new domain for the metal and plasma zones.
4. When the zinc vapour escapes into the keyhole, solve equations (46)–(48) under the associated boundary conditions in equations (49)–(54) to obtain velocity distributions for the zinc vapour.

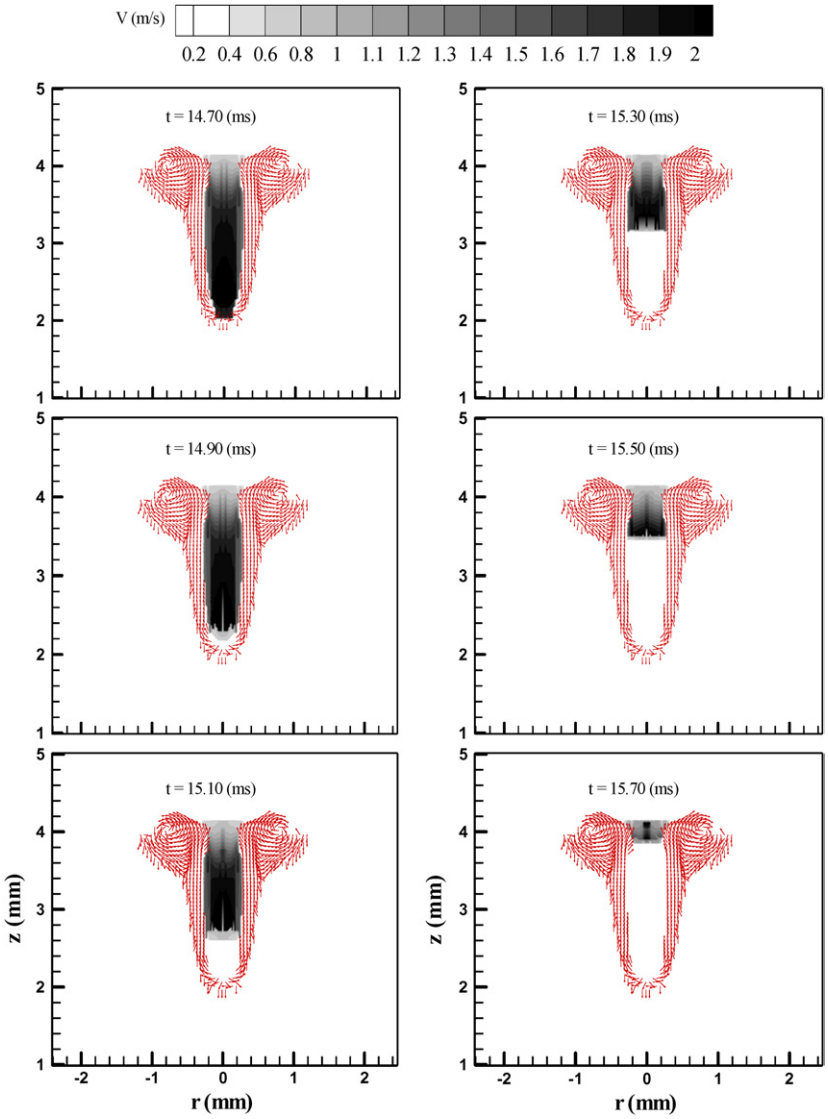

Figure 7. Continued.

5. Update boundary conditions for the metal and plasma zones.
6. Advance to the next time step and back to step 1 until the desired time is reached.

The techniques for solving equations (1)–(4), equation (34) and equations (46)–(48) are given by Wang and Tsai [22]. Following the marker-and-cell (MAC) scheme, the r- and z-velocity components are located at cell face centres on lines of constants r and z, respectively; while the pressure, VOF function, temperature and absorbed laser flux are located at cell centres. Since the temperature and pressure field change more dramatically near the keyhole, a non-uniform grid system with 127 × 202 points is used for the total computational domain of 10.0 mm × 5.0 mm, in which smaller grids are concentrated near the keyhole and larger grids for other parts. Due to the axis-symmetry of the domain, only half of the grid points were used in the calculation. Calculations were executed on the Dell Optiplex GX270 workstations with Linux-Redhat 9.0 OS and it took about 7 h of CPU time to simulate about 100 ms of real-time welding. The average time step is 10^{-4} s and the smallest time step is about 10^{-6} s.

4. Results and discussion

The thermophysical properties and welding conditions used in the present study are summarized in table 1. In this study, a CO_2 laser has been used and the pulse shape is shown in figure 2. The laser power at the focus is 2.0 kW, the diameter at the focus is 500 μm and the laser energy is in a Gaussian distribution. For the target materials, two pieces of 304 stainless steel sheet (in lap joint configuration) with zinc coating containing 100 ppm of sulfur with a thickness of 2.0 mm and radius of 10.0 mm have been selected. The thickness of zinc coating is 10 μm.

4.1. Keyhole formation

Figure 3 shows a sequence of weld pool evolution during the keyhole formation. The corresponding temperature

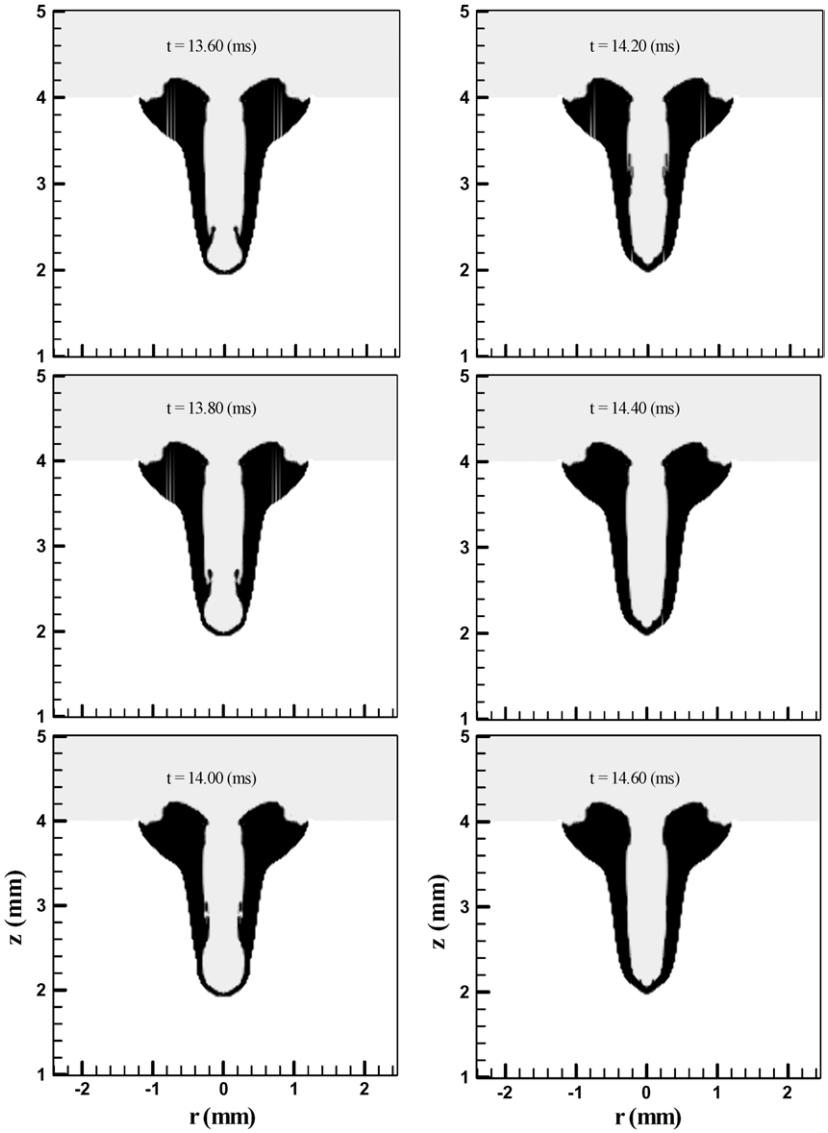

Figure 8. The weld pool variation during zinc vapour escaping.

and velocity distributions are shown in figures 4 and 5, respectively.

As shown in figure 2, the laser power is increased from 0 to 2.0 kW gradually within 1.0 ms. At this stage, the laser energy is mainly used to heat up the base metal. With the increase in the base metal temperature, a small and shallow weld pool appears under the laser beam. As the laser light continues to irradiate the base metal, part of the liquid metal is vaporized causing the formation of the vapour-induced recoil pressure. This recoil pressure starts to push down the liquid in the weld pool. Since it takes a while to accelerate the liquid from the static condition, the fluid flow in the weld pool is not significant and the surface of the weld pool is nearly flat at $t = 1.0$ ms. When more and more laser energy is absorbed and the temperature on the weld pool surface increases, the recoil pressure becomes stronger and it pushes the liquid metal to flow downwards. As shown in figure 5, a strong downward flow begins to appear at the bottom of the keyhole. Meanwhile, due to the Gaussian distribution of laser intensity, the temperature difference along the surface of the weld pool is very large as shown in figure 4, which leads to a high positive temperature-dependent Marangoni shear stress along the weld pool surface. This Marangoni shear stress combined with the recoil pressure squeezes the liquid metal to flow upwards along the keyhole wall. So a shallow keyhole is formed.

When $t > 6.0$ ms, since a shallow keyhole is formed, some metal vapour is trapped in the keyhole. The laser light interacts with this metal vapour and part of the laser energy is absorbed by the metal vapour. The temperature of the metal vapour increases very quickly due to its small heat capacity. When its temperature is over 8000 K, some kind of ionization occurs and laser-induced plasma is generated. With the formation of the plasma, much more energy is absorbed via the IB absorption, so that the temperature of plasma increases very quickly. As shown in figure 4, the temperature of the plasma inside the keyhole can reach as high as 19 000 K. This hot plasma inside the keyhole radiates the keyhole wall to a very high temperature to produce a stronger recoil pressure which helps the keyhole depth to increase very quickly. Meanwhile, formation of the

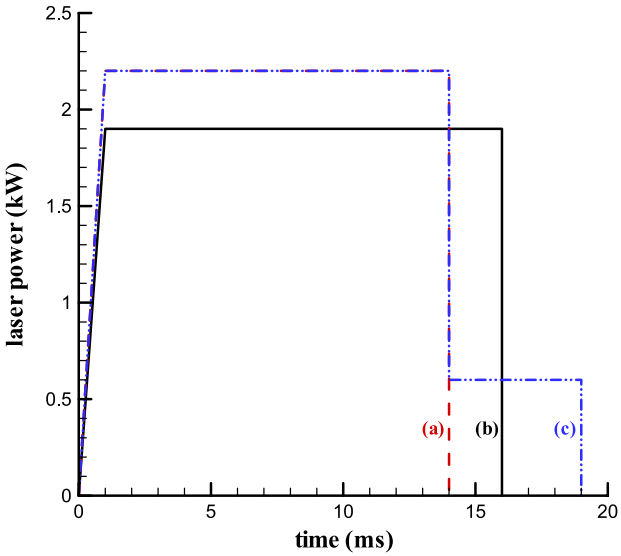

Figure 9. Laser pulse used for (*a*) producing a thick weld pool, (*b*) producing a thin weld pool and (*c*) preventing welding defects.

keyhole also enhances the laser light absorption through a mechanism called multiple reflections which brings more laser energy to the keyhole wall and this leads to a further higher recoil pressure. Moreover, as the keyhole deepens, the times of multiple reflections increase. Hence, at $t = 13.0$ ms, a deep keyhole is formed.

4.2. Zinc vapour formation and escaping via keyhole

Figure 6 shows the zinc coating melting and zinc vapour formation processes. Since the melting point of the zinc is much less than that of the steel, according to the temperature distributions, the temperature at the interface location is higher than the melting point of the zinc but lower than that of the steel; hence, at $t = 13.2$ ms, although the depth of the keyhole has not reached the interface, part of the zinc coating begins to melt in the interface and there is still some solid metal above which is un-melted steel. With the increase in temperature, the liquid zinc begins to vaporize to form zinc vapour. In the lap joint configuration, since there is no exit for this zinc vapour to escape, the zinc vapour is trapped and accumulated to a very high pressure with the continuous increase in the temperature.

As the laser continues to irradiate and the keyhole reaches to a certain depth, the static pressure of the liquid metal cannot sustain the high pressure of the trapped zinc vapour; the high-pressure zinc vapour breaks the liquid metal layer above and escapes from the keyhole. Figure 7 shows the escaping process of the zinc vapour via the keyhole. As shown in the figures, the high-pressure zinc vapour first bursts into the keyhole and uses it as a route to escape. When the zinc vapour reaches the keyhole exit, it then dissipates into the outside air. The escaping time period is very short and the escaping speed of the zinc vapour is very fast. As shown in the figures, the escaping speed of the zinc vapour is in the order of 200 cm s^{-1} and the escaping time is around 1.0 ms.

Figure 8 shows the keyhole shape variation during the zinc vapour escaping process. Since the zinc vapour is at very high pressure and its velocity is very high, it severely interacts with the weld pool, especially with the weld pool near the interface. As shown in figure 8, the escaping zinc vapour interacts with the weld pool and damages its continuity early in the process. Since the weld pool is thick in this case, the hydrostatic pressure of the liquid metal can make the weld pool recover its continuity and the zinc vapour can dissipate into the air before the keyhole collapses. Hence, the welding defects related with zinc vapour, such as undercut and porosity, are avoided. So, in the case as shown in figure 8, keyhole has been used as an effective way to vent the zinc vapour, which verifies some experimental observations [17]. Also, similar phenomenon has been found by Girard *et al* [38] and Kaplan *et al* [39] in their experiments.

4.3. Defect formation

As shown above, since the zinc vapour strongly interacts with the weld pool during its escaping process, in some cases it can strongly damage the weld pool shape and severely affect the weld pool dynamics, which causes a lot of welding defects, such as splashing, undercut and porosity. From the velocity field distribution of the interacting weld pool region, high velocities were found in the melt, which may cause irregular collapse of the keyhole and corresponding porosity. The following studies were conducted to understand the defect formation mechanisms in laser welding of zinc-coated steels.

4.3.1. Thin weld pool. In this case the laser power is 1.9 kW and its pulse shape is given in figure 9. Figure 10 shows a sequence of liquid metal region evolution during keyhole collapse.

As shown in figure 10 at $t = 16.2$ ms, since the welding pool is thin, when the zinc vapour escapes from the keyhole, most of the liquid metal at the lower part of the keyhole was pushed upwards. When the laser power is shut off at $t = 16.0$ ms, there is no heat input from the laser. Also, since the heat capacity of the plasma is very small, the plasma inside disappears very quickly and brings very little heat input to the keyhole wall. Meanwhile, the heat conduction from the keyhole wall to the surrounding metal is strong. Hence, at $t = 16.5$ ms the liquid metal at the bottom of the keyhole is totally solidified. Meanwhile, the liquid metal at the top of the keyhole is flowing upwards and outwards to the corner of the keyhole because of the strong push from the zinc vapour. When the liquid metal is pushed to the top corner of the keyhole, since the weld pool is thin, which means the heat capacity of the liquid metal is small, a certain amount of liquid metal at the corner solidifies very quickly due to the strong heat loss and it cannot flow downwards and inwards to the centre of the keyhole. So a crater is found at the corner at $t = 23.8$ ms. After the shut off of the laser beam at $t = 16.0$ ms, the laser induced recoil pressure also decreases very quickly. The surface tension and hydrostatic pressure drive the liquid metal on the top to fill back into the keyhole. Meanwhile, due to the strong heat conduction loss to the surrounding solid metal, from $t = 23.8$ ms to $t = 36.4$ ms, the liquid region shrinks, especially at the top because most of the hot liquid metal there is flowing downwards and the velocity of the downward-flowing liquid metal drops very quickly. Finally, at $t = 49.8$ ms, the downward-flowing liquid metal completely solidifies before it

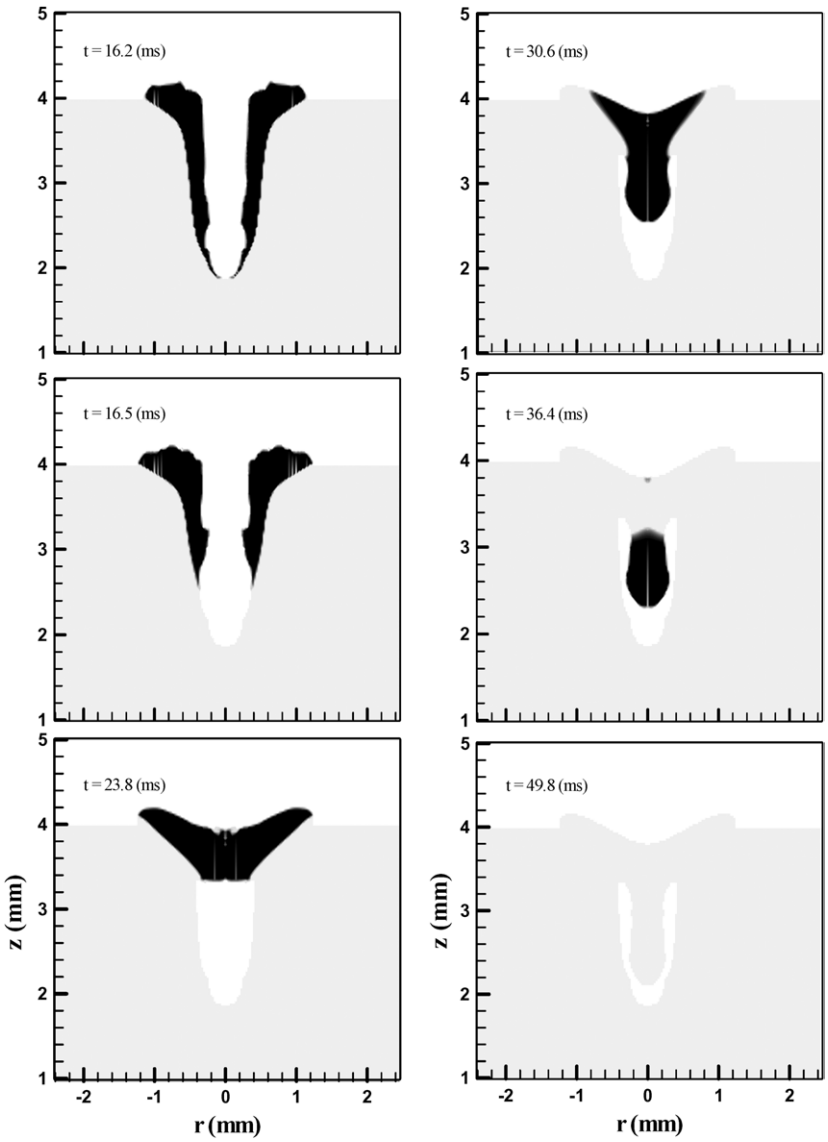

Figure 10. A sequence of liquid metal evolution during keyhole collapse when weld pool is thin.

can reach the bottom of the keyhole, which leaves a void at the tip of the weld.

On the top surface of the weld bead, an undercut is clearly found. As mentioned earlier, a certain amount of liquid metal is accumulated and solidified at the corner. This part of the liquid cannot flow back to the centre. Meanwhile, part of the remaining liquid metal in the centre moved downwards to fill the void and this part of the liquid metal cannot flow back upwards to the top surface during the solidification process, so an undercut was formed at the centre on the top surface at $t = 49.8$ ms.

4.3.2. Thick weld pool. The laser power used in this case is 2.2 kW and the laser pulse shape is shown in figure 9. Figure 11 shows the metal evolution during the keyhole collapse process. As shown, the welding pool is relatively thick. At $t = 15.2$ ms, considerable liquid metal has accumulated on the top of the keyhole. Since there is less liquid metal at the bottom of the keyhole wall, this part of the liquid metal can be more easily pushed up by the zinc vapour. Also, due to the strong heat conduction loss there, at $t = 17.8$ ms the liquid metal at the bottom of the keyhole totally solidified. On the top, contrary to the previous case, since there is considerable liquid metal accumulated there, the escaping zinc vapour still affects the weld pool dynamics, but it does not damage the weld pool shape as violently as in the previous case. When the laser power is shut off, with the combined actions of the surface tension and hydrostatic force, the large amount of liquid metal on the top tends to flow downwards and inwards to refill the keyhole. Meanwhile, due to the strong heat loss, the hot liquid metal is cooled down very quickly when it flows downwards along the keyhole wall, especially for the liquid metal at the bottom of the keyhole. As shown at $t = 48.2$ ms, the bottom part of the liquid metal completely solidified. Although, there is still some liquid metal above, it cannot reach the bottom of the keyhole due to the solidified metal in between. As a result, a void is formed at the root of the keyhole.

In the previous case, a very obvious crater was found at the top corner of the weld bead and a very serious slumping

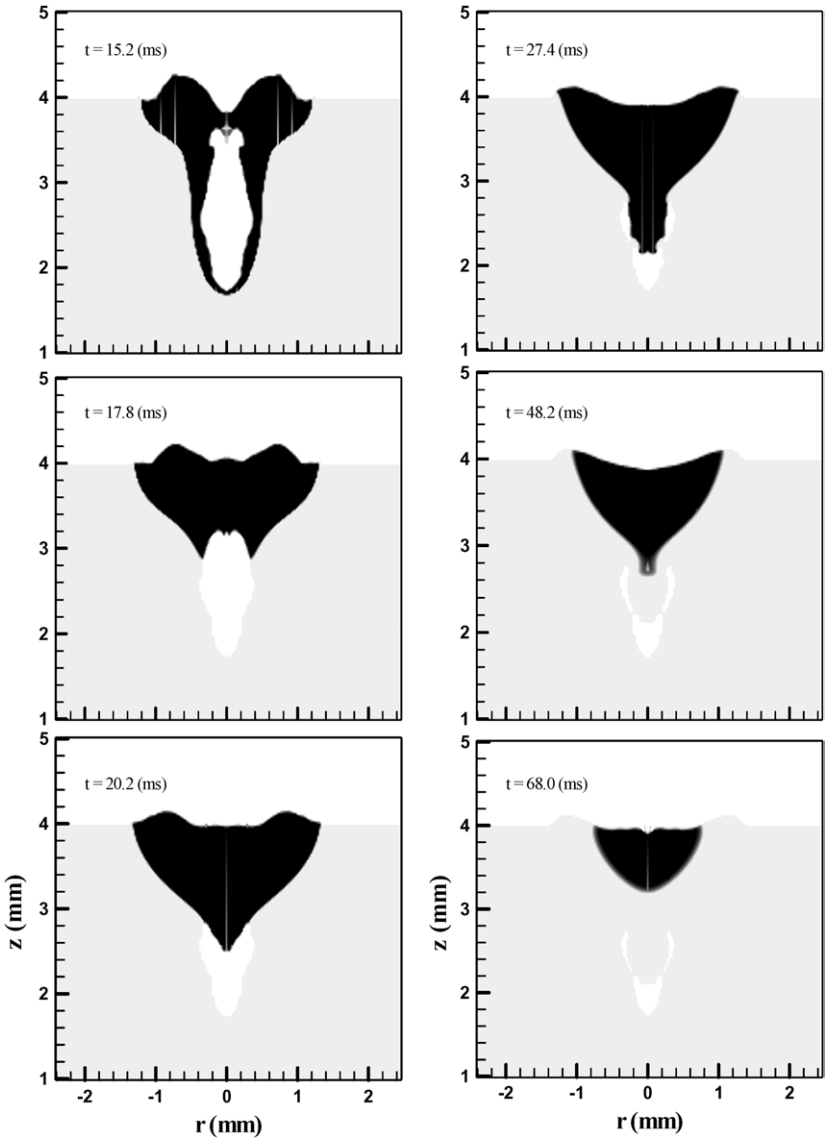

Figure 11. A sequence of liquid metal evolution during keyhole collapse when weld pool is thick.

appeared in the centre of the weld bead. In the present case, as shown in figure 11 at $t = 15.2$ ms, since there is considerable liquid metal with a high temperature at the corner and the velocity of the liquid metal at the top is at rather high values, some hot liquid metal in the centre can flow to the corner. Thus, the liquid metal at the corner does not quickly solidify and it can exist as a liquid phase for a period of time. After the shut-off of the laser power, with the action of the surface tension and hydrostatic force, the liquid metal at the corner flows inwards to the centre. When the liquid metal flows back to the centre, the surface of the weld pool becomes flatter, which causes a decrease in the surface tension. With the decrease in surface tension, most of the liquid metal flowing back to the centre does not flow back to the corner again. So, no obvious crater is formed at the corner. Although, with the action of the hydrostatic force, part of the liquid metal in the centre flows downwards to fill the keyhole, due to the quick solidification process only part of the liquid metal can flow downwards and most of the liquid metal stays at the top of the weld until it fully solidifies, so no undercut appears at the centre in the final weld bead.

4.4. Defect prevention by pulse control

As shown above, the quick solidification process after the shut-off of the laser power causes the void defect. Controlling the laser pulse shape is proposed to delay the solidification process, so that the back-filling time for the hot liquid metal on the top can be increased. For the previous two cases, the laser power is shut off completely after the keyhole formation, and this caused the liquid metal at the bottom to quickly solidify. In this case, the laser power shape used is shown in figure 9. As shown, the laser power is not completely shut off at $t = 14.0$ ms instead, it is decreased to a smaller value of 0.6 kW and is held for 5.0 ms. The corresponding sequence of weld pool evolution, the velocity evolution and the temperature evolution are shown in figures 12–14.

As shown in figure 12, after the shut off of the laser beam, the reduced laser power continues to heat the keyhole surface,

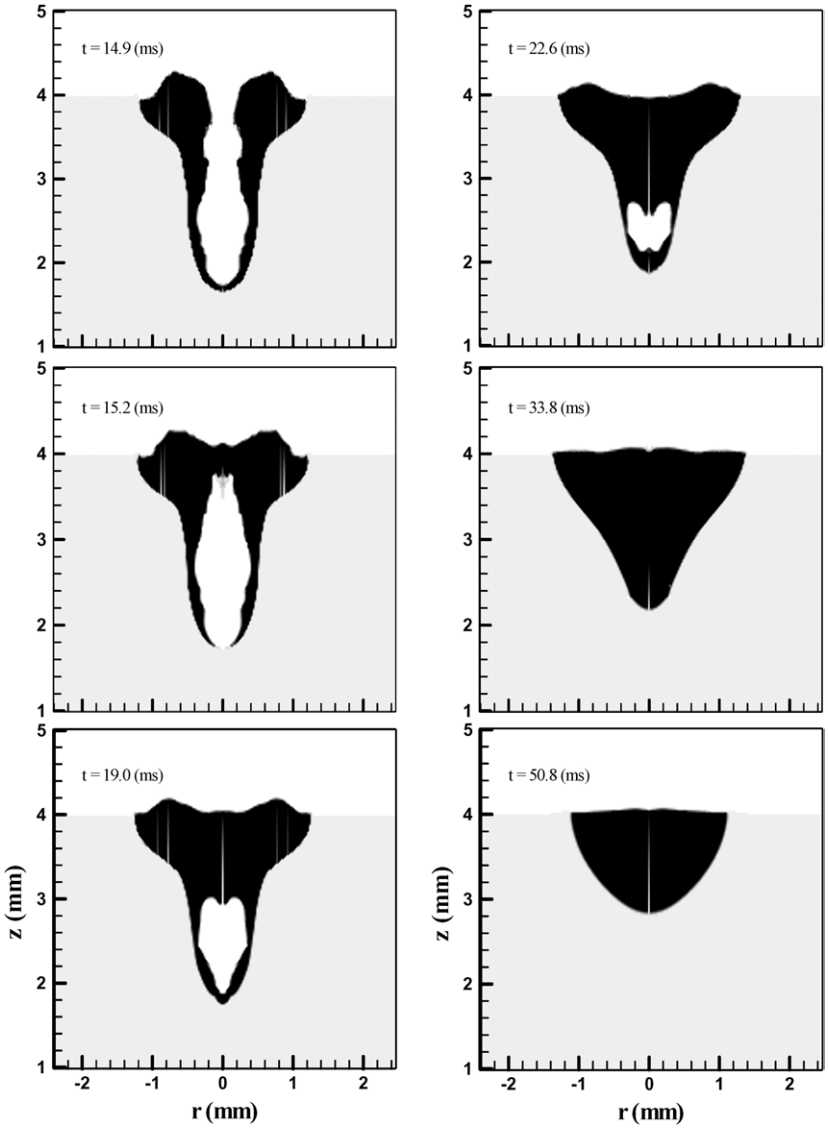

Figure 12. A sequence of liquid metal evolution during void elimination by laser pulse control.

which keeps the liquid metal at the bottom of the keyhole from solidifying at $t = 14.9$ ms. When the liquid metal on the top of the keyhole collapses to the centre and prevents the laser light from reaching the bottom surface of the keyhole, the multiple reflections on the keyhole wall reflect some laser energy inside the keyhole which helps keep the liquid metal at the bottom of the keyhole in liquid status. As shown in figure 13, the temperature on the bottom of the keyhole is still high, so it keeps the liquid metal there from solidifying quickly. At $t = 19.0$ ms since the laser is still on, although its energy density has been decreased to 0.6 kW, this additional energy can keep the temperature of the liquid metal on the top of the keyhole at a high value. During the back-filling process, since there is considerable liquid metal accumulation on the top of the keyhole and its viscosity is small due to its high temperature, with the combined actions of surface tension and hydrostatic force, as shown in figure 14, the downward velocity of the liquid metal is accelerated to a higher value compared with that in the previous two cases. At $t = 33.8$ ms, this high speed and high temperature liquid can reach the bottom of the keyhole before solidification, so the void at the root of the keyhole is eliminated.

After that, due to the shut-off of the laser power, the temperature of the liquid metal decreases and its velocity decreases accordingly. As shown in figure 14 at $t = 50.8$ ms, the velocities of the liquid metal drop to very small values and the liquid metal almost stops flowing and the surface of the weld pool turns flat. Meanwhile, the heat in the liquid metal is conducted into the surrounding solid metal and the solidification process happens very quickly. Finally, when the liquid metal completely solidifies, a sound weld without pores is achieved. Although, there may be some very tiny pores due to the small amount of zinc vapour formed in the process, since these are very tiny, they do not affect the overall quality of the weld bead and the study of these pores is not discussed here.

5. Conclusions

A mathematical model has been developed for laser welding of zinc-coated steels by using the VOF technique and the

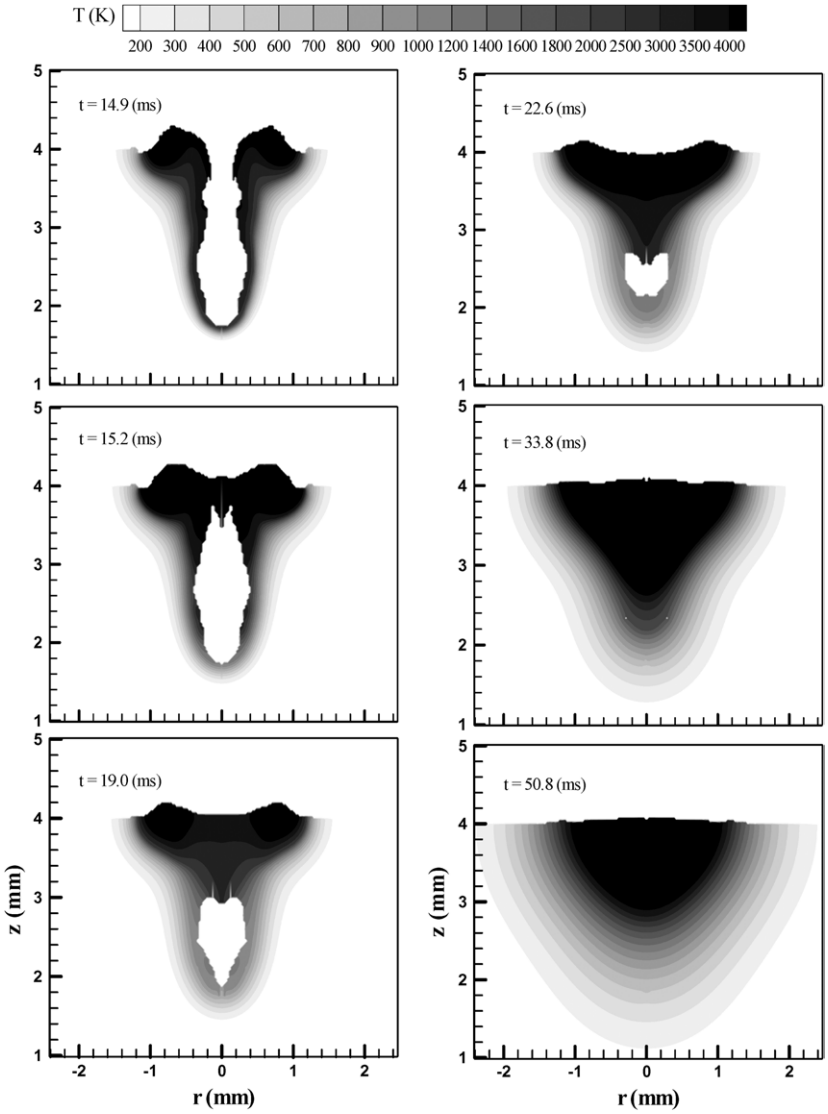

Figure 13. The corresponding temperature distributions as shown in figure 12.

continuum formulation. Using the model, the keyhole formation process has been investigated including the effects of multiple reflections, laser-induced evaporation and ionization. The transient keyhole shape, weld pool shape, velocity and temperature distributions both in the weld pool and the plasma have been calculated. Also, the formation and escaping processes of zinc vapour have been studied. These studies reveal that the evaporation-dependent recoil pressure is the main driving force for the keyhole formation. The laser-induced plasma formation, radiation and multiple reflections on the keyhole wall are important factors during the keyhole formation process. Zinc vapour interacts with the weld pool during its escape. By controlling laser power and pulse duration, the keyhole can be used as an effective venting path for the zinc vapour.

The defect formation mechanisms are also investigated by using this model. During the laser welding of zinc-coated steels, when the weld pool is thin, due to the strong interaction between zinc vapour and weld pool and the quick solidification process after the shut-off of laser power, a large void is found in the final weld. Also, an undercut at the top surface and a crater at the corner are easily found. The crater is caused by quick solidification at the corner and an undercut is due to insufficient liquid metal to refill the top surface of the centre during solidification. When the weld pool is thick during the welding process, the undercut at the top surface of the weld can be eliminated, but a void still occurs at the tip of the weld due to quick solidification. If the laser power is held at a moderate value for a while before its complete shut off, this extra energy can be used to delay the solidification of the liquid metal at the bottom of the keyhole and accelerate the velocity of back-filling liquid metal from the central top. A sound weld bead with no voids inside the solidified metal can be achieved. The phenomena revealed by the proposed model are in good agreement with the experimental observations [17, 38, 39], which indicate the proposed mathematical model can be used as a solid base for future studies. In future studies, more realistic assumptions, such as flow of keyhole plasma and compressibility of zinc vapour, will be considered to further improve the accuracy of the model.

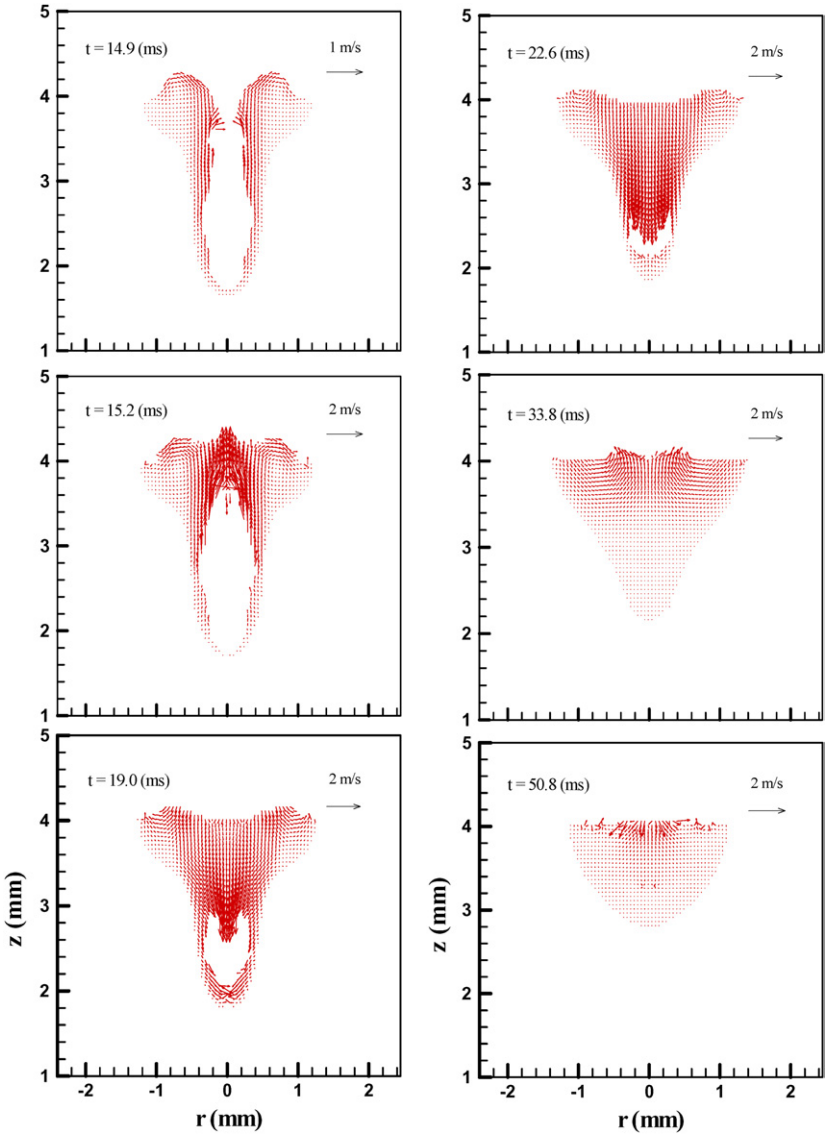

Figure 14. The corresponding velocity distributions as shown in figure 12.

Acknowledgments

The work was partially supported by the U.S. Army Research Office under Grant Number DAAG55-98-1-0097 and General Motors Corporation.

References

[1] Tzeng Y F 2000 *JSME Int. J.* **43** 47
[2] Denney P and Xie J 2000 *Proc. ICALEO (Dearborn, MI)* vol 91 p A-1
[3] Akhter R, Steen W M and Watkins K G 1991 *J. Laser Appl.* **3** 9
[4] Akhter R, Steen W M and Cruciani D 1988 *Proc. 5th Int. Conf. on Lasers in Manufacturing (LIM5, Stuttgart)* (IFS Publications) p 195
[5] Graham M P, Hirak D M, Kerr H W and Weckman D C 1996 *J. Laser Appl.* **6** 212
[6] Heyden J, Nilsson K and Magnusson C 1989 *Proc. 6th Int. Conf. on Lasers in Manufacturing (LIM6, Birmingham, UK)* (IFS Publications) p 93
[7] Abdel-Monew E 1997 *Steel Res.* **68** 546
[8] Williams S W, Salter P L, Scott G and Harris S J 1993 *Proc. 26th Int. Symp. on Automotive Technology and Automation* (Aachen, 1993) p 49
[9] Ream S 1991 *Laser Applications in Materials Processing and Manufacturing (Society of Manufacturing Engineering) (Berlin: Springer)*
[10] Pecas P, Henrique M, Miranda R M and Quintino L 1995 *Opt. Quantum Electron.* **27** 1193
[11] Kennedy S C and Norris I M 1989 *International Congr. and Exposition (Dearborn, MI) SAE Technical Paper 890887*
[12] Dasgupta A and Mazumder J 2000 *Proc. ICALEO (Dearborn, MI)* vol 91, p 38
[13] Tzeng Y F 2000 *J. Mater. Process. Technol.* **100** 163
[14] Katayama S and Matsunawa A 2000 *8th Annual Automotive Laser Applications Workshop (Anaheim, CA)*
[15] Gualini M M S 2001 *Proc. ICALEO (Orlando, FL)* vol 93, p 511
[16] Gu H P and Mueller R 2001 *Proc. ICALEO* vol 93, p 304
[17] Katayama S, Yushen W U and Matsunawa A 2001 *Proc. ICALEO (Orlando, FL)* vol 93, p 520
[18] Xie J and Denney P 2001 *Weld. J.* **80** (6) 59
[19] Matsunawa A, Kim J D, Seto N, Mizutani M and Katayama S 1998 *Taiwan Int. Welding Conf. (Tapei)*

[20] Katayama S, Kohsaka S, Mizutani M, Nishizawa K and Matsunawa A 1993 *Proc. ICALEO (Orlando, FL)* vol 77, p 487
[21] Kothe D B, Mjolsness R C and Torrey M D 1991 *Ripple: A Computer Program for Incompressible Flows with Free Surfaces* LA-12007-MS (Los Alamos National Laboratory)
[22] Chiang K C and Tsai H L 1992 *Int. J. Heat Mass Transfer* **35** 1763
[23] Miyamoto I, Ohmura E and Maede T 1997 *Proc. ICALEO (San Diego, CA)* vol 83, p 210
[24] Dowden J, Postacioglu N, Davis M and Kapadia P 1987 *J. Phys. D: Appl. Phys.* **20** 36
[25] Wang Y and Tsai H L 2001 *Int. J. Heat Mass Transfer* **44** 2067
[26] Semk V V, Hopkins J A, McCay M H and McCay T D 1994 *Proc. SPIE* **2500** 641
[27] Semak V V, Knorovsky G A, MacCallum D O and Roach R A 2006 *J. Phys. D: Appl. Phys.* **39** 590
[28] Sahoo P, DeBroy T and Mcnallan M J 1988 *Metall. Trans.* **19B** 483
[29] Choo R T C, Szekely J and David S A 1992 *Metall. Trans.* **23B** 371
[30] Knight C J 1979 *AIAA J.* **17** 519
[31] Semak V and Matsunawa A 1997 *J. Phys. D: Appl. Phys.* **30** 2541
[32] Zacharia T, David S A and Vitek J M 1991 *Metall. Trans.* B **22B** 233
[33] Raizer Y P 1977 *Laser-Induced Discharge Phenomena* (New York: Consultants Bureau)
[34] Spitzer L 1962 *Physics of Fully Ionized Gases* (New York: Wiley)
[35] Kogelnik H and Li T 1966 *Appl. Opt.* **5** 1550
[36] Siegel R and Howell J R 1992 *Thermal Radiation Heat Transfer* 3rd edn (New York: Hemisphere) (chapter 13)
[37] Ho R, Grigoropoulos C P and Humphrey J A C 1996 *J. Appl. Phys.* **79** 7205
[38] Girard K, Jouvard J M and Naudy P H 2000 *J. Phys. D: Appl. Phys.* **33** 2815
[39] Kaplan A, Mizutani M, Katayama S and Matsunawa A 2002 *J. Phys. D: Appl. Phys.* **35** 1218